An experimental study of turbulent relative dispersion models

Nicholas T. Ouellette, Haitao Xu, Mickaël Bourgoin, Eberhard Bodenschatz

New Journal of Physics
The open-access journal for physics

An experimental study of turbulent relative dispersion models

Nicholas T Ouellette[1,2,4], **Haitao Xu**[1,2], **Mickaël Bourgoin**[3] **and Eberhard Bodenschatz**[1,2]

[1] Laboratory of Atomic and Solid State Physics, Cornell University, Ithaca, NY 14853, USA
[2] Max Planck Institute for Dynamics and Self-Organization, 37077 Göttingen, Germany
[3] Laboratoire des Écoulements Géophysiques et Industriels—C.N.R.S. (U.M.R. 5519), BP 53-38041, Grenoble Cedex 9, France
E-mail: nto2@cornell.edu

New Journal of Physics **8** (2006) 109
Received 12 April 2006
Published 23 June 2006
Online at http://www.njp.org/
doi:10.1088/1367-2630/8/6/109

Abstract. We report measurements of the spreading rate of pairs of tracer particles in an intensely turbulent laboratory water flow. We compare our measurements of this turbulent relative dispersion with the longstanding work of Richardson and Batchelor, and find excellent agreement with Batchelor's predictions. The distance neighbour function, the probability density function of the relative dispersion, is measured and compared with existing models. We also investigate the recently proposed exit time analysis of relative dispersion.

[4] Author to whom any correspondence should be addressed.

1367-2630/06/010109+23$30.00

Contents

1. Introduction

Fluid flows in nature or in industry are rarely laminar; much more often, they are turbulent. Turbulent flows are, however, very difficult to analyse. We have known the Navier–Stokes equations that govern fluid flow for well over a century, but we have made little progress in using them to understand turbulence. These difficulties combined with its prevalence in nature led Feynman to call turbulence one of the greatest unsolved problems in physics [1].

The Navier–Stokes equations are very difficult to solve directly on the computer for very intense turbulence or complex boundary conditions, since turbulence is typified by dynamics over a huge range of relevant length and timescales. Researchers therefore commonly turn instead to phenomenological statistical models. The most common and powerful of these is Kolmogorov's 1941 scaling theory [2], which predicts scaling laws for many different statistical quantities in turbulent flow.

Kolmogorov distinguished three regimes of turbulence. At large length and time scales, energy is transferred from the forcing of the flow into the turbulence. At these scales, larger than the correlation length L and correlation time T_L of the turbulent velocity field, the turbulence statistics are expected to depend on the exact forcing mechanism and geometry of the flow. For very intense turbulence, Kolmogorov broke the smaller length and time scales into two regimes. At intermediate scales, he suggested that turbulence statistics should have a universal form independent of the large-scale flow, and that the only relevant flow parameter should be the rate of turbulent energy dissipation per unit mass ϵ. This regime is known as the inertial range. At small enough scales, however, molecular viscosity should begin to play a role. Below the Kolmogorov length and time scales η and τ_η, defined as the scales at which the viscous forces balance the inertial forces, Kolmogorov proposed that turbulence statistics will have different universal forms that depend on both ϵ and the kinematic viscosity ν.

Kolmogorov's model is only expected to be valid for very intense turbulence, typified by large values of the Reynolds number. Defined as $Re \equiv uL/\nu$, where u is the root mean square

turbulent velocity, the Reynolds number measures the ratio of inertial and viscous forces. In this work, we report the Reynolds number based on the Taylor microscale, $R_\lambda = \sqrt{15Re}$.

Most of our knowledge of turbulence comes from so-called Eulerian measurements, made at points fixed with respect to some laboratory reference frame. In recent years, however, Lagrangian measurements that follow the motion of individual fluid elements have become possible. A central component of the Lagrangian description of turbulence is the relative motion of pairs of fluid elements. Termed turbulent relative dispersion, the spreading of fluid element pairs is the fundamental mechanism underlying all turbulent mixing and transport. Therefore, without understanding turbulent relative dispersion, we cannot hope to have a full understanding of problems as diverse as pollutant or bioagent transport in the atmosphere, the growth rate of water droplets in warm clouds, or the mixing of fuel in a combustion engine.

Researchers have proposed many models of turbulent relative dispersion, beginning with Richardson's work in the 1920s [3]. Due to the difficulty of Lagrangian measurements, however, there have been little experimental data that can be used to test these models. We have measured the spreading rates of passive tracer particles in an intensely turbulent laboratory water flow (Reynolds numbers up to $R_\lambda = 815$). We have previously reported the observation of a scaling range consistent with Batchelor's predictions [4]; here, we apply several alternative models of turbulent relative dispersion to our data.

In section 2, we describe our experimental setup and particle tracking algorithms. We discuss the traditional Richardson and Batchelor models of relative dispersion in section 3. In section 4, we discuss possible higher-order corrections to these models involving the relative velocity and acceleration of the particles. Section 5 describes our measurements of the probability density function (PDF) of turbulent relative dispersion, commonly known as the distance neighbour function. Finally, in section 6, we investigate the recently proposed exit time analysis for relative dispersion.

2. Experimental details

We generated turbulence by counter-rotating two baffled discs in a closed plexiglass cylindrical chamber containing 120 litres of water, described in detail previously [5, 6]. While this flow is both anisotropic and inhomogeneous, it can be used to achieve very high Reynolds numbers in a relatively small amount of laboratory space. In addition, the size of the apparatus makes it well-suited to Lagrangian measurements; in wind tunnels or other configurations with strong mean flows, it is significantly more difficult to follow tracer particles for long periods of time [7].

We here describe the Lagrangian particle tracking algorithms we use (subsection 2.1), the optical setup and cameras (subsection 2.2), and the calibration procedure (subsection 2.3), and finally show some of the parameters of our experiments (subsection 2.4).

2.1. Lagrangian particle tracking

Particle tracking is the most robust Lagrangian measurement technique in use in fluid mechanics today. In this technique, the flow is seeded with very small tracer particles that behave approximately as fluid elements. These tracers are typically imaged optically, although acoustic systems have also been developed [8]; acoustic systems, however, directly measure the tracer

velocities, and the velocity trajectories must then be integrated to give the tracer positions. Optical three-dimensional Lagrangian particle tracking can broadly be broken into three steps. First, the particle images must be identified from the recorded camera frames and their centres must be located, ideally with sub-pixel resolution. Next, the two-dimensional coordinates of the particle centres found from each camera must be correlated to produce three-dimensional particle positions. This stereomatching step has the added benefit of filtering out spurious particles, since they will not match images from the other cameras. Finally, the three-dimensional coordinates of the particles must be followed in time, generating particle tracks. An analysis of Lagrangian particle tracking algorithms was given by Ouellette *et al* [9]; we here briefly describe the particular methods used in the experiments reported in this work.

Particle images were identified by assuming that every local intensity maximum above a small threshold corresponded to a particle. The particle centres were then determined by fitting two one-dimensional Gaussians to the particle image, one horizontally and one vertically. In practice, this requires only the intensities of the local maximum pixel and the pixels directly adjacent to it horizontally and vertically. Labelling the horizontal coordinates x_1, x_2 and x_3, where x_2 is the coordinate of the local maximum, we can solve for the coordinate x_c of the centre of the particle analytically, obtaining

$$x_c = \frac{1}{2}\frac{(x_1^2 - x_2^2)\ln(I_2/I_3) - (x_2^2 - x_3^2)\ln(I_1/I_2)}{(x_1 - x_2)\ln(I_2/I_3) - (x_2 - x_3)\ln(I_1/I_2)}, \tag{1}$$

where I_1, I_2 and I_3 are the pixel intensities. The vertical coordinate of the particle centre is defined analogously. This method provides the coordinates of the particle centres with an accuracy of 0.1 pixels or better [9], as well as being efficient: since the cameras are digital, all possible logarithms needed for (1) can be precomputed and stored.

After the locations of the particle centres are determined in the images from each camera, the sets of two-dimensional particle coordinates must be correlated to generate three-dimensional particle images. Since the tracers have no distinguishing characteristics, the only information that can be used to match the particles is the photogrammetric condition that, for each camera, the camera projective centre, the particle coordinates on the image plane, and the particle coordinates in the laboratory frame must be collinear [10]. The stereomatching algorithm we use is straightforward. Consider a particle image p_i on one detector. We project a line from the perspective centre of the camera, determined by calibration of the system, through p_i. We then in turn project this line onto the image planes of the other cameras. Particle images on these images planes that fall within a small tolerance are considered possible matches to p_i. In this fashion, a list of possible matches for p_i is constructed for every other camera in the system. This process is then repeated for every particle image on every detector. The lists are then checked for consistency, and the three-dimensional coordinates are found.

Once the three-dimensional coordinates have been determined, the particles must be tracked in time. We use a four-frame predictive algorithm to solve the particle tracking problem. Using the position of a particle in frames n and $n - 1$, we can estimate its velocity and thereby its probable position in frame $n + 1$. We then investigate all particles in a small volume around the estimate in frame $n + 1$. For each of these particles, we estimate both a new velocity and an acceleration, and predict a position in frame $n + 2$. To extend the track, we choose the particle in frame $n + 1$ that produced an estimate closest to a real particle in frame $n + 2$. We have previously shown that this algorithm is both robust and accurate even in intensely turbulent flow [9].

2.2. Imaging system

Optically resolving particle motions in intense turbulence requires an imaging system with a very high temporal resolution. For efficient and accurate particle tracking, such a system must over-resolve the Kolmogorov timescale $\tau_\eta = \sqrt{\nu/\epsilon}$, the smallest turbulent timescale, especially when time derivatives of the particle motion are desired. τ_η is typically very short; for example, in our water flow at $R_\lambda = 815$, the highest Reynolds number reported here, $\tau_\eta = 0.544$ ms. Making at least ten measurements per τ_η thus corresponds to a minimum imaging rate of 18 000 frames per second; an even faster camera is required to make very accurate measurements. Previously, due to the lack of commercial cameras capable of recording images at these speeds, we adapted the silicon strip detectors used in the vertex detectors of high-energy particle accelerators for use in Lagrangian particle tracking [6, 11, 12]. These strip detectors, however, have proved to be unsuitable for measuring multiple particles simultaneously. For the work presented here, we have therefore used commercial high-speed cameras. Recent advances in imaging technology have led to commercial cameras with significantly higher imaging rates than were previously available. We have used the Phantom v7.1 CMOS camera from Vision Research, Inc., which is capable of recording images at a rate of 27 000 frames per second at a resolution of 256 × 256 pixels. Since these cameras have a two-dimensional sensor, as opposed to the one-dimensional strip detectors, we can use them to record the trajectories of several hundred particles simultaneously [9]. These particle tracks can then be used to study multiparticle statistics such as the relative dispersion discussed here.

Just as the imaging rate must be faster than the Kolmogorov timescale for accurate measurements, so must the tracer particle size be smaller than the corresponding length scale in order to ensure that the tracer behaves just like a real fluid element. The Kolmogorov length scale $\eta = (\nu^3/\epsilon)^{1/4}$ is the smallest turbulent length scale; the flow at scales smaller than η is smooth and laminar. We use transparent polystyrene microspheres with a diameter of 25 μm and a density 1.06 times that of water.[5] These particles are smaller than or comparable to η for all the Reynolds numbers reported in this work (see table1), and have previously been shown to act as passive tracers in this flow [6].

A sketch of our experimental apparatus and optical setup is shown in figure 1. We used three Phantom cameras arranged in a single plane with an angular separation of roughly 45°. With three cameras, we were able to measure the full three-dimensional positions of the tracer particles. While two cameras are in principle sufficient for determining three-dimensional positions, Dracos [13] has shown that at least three cameras are needed to resolve the ambiguities that can arise when the images of the particles from each camera are correlated to generate three-dimensional coordinates. Eight round, flat windows were glued around the centreline of the tank with an angular separation of 45°; the cameras were aligned with these windows to avoid lensing by the cylindrical walls of the tank. The cameras were fitted with 60 mm Nikon lenses with an f-number of 11.

In the experiments presented here, we have used two Q-switched, frequency-doubled Nd:YAG lasers for illumination. One of the lasers, pumped by flashlamps, had a peak output power of roughly 60 W, while the other, pumped by diode arrays, had a peak power of roughly 90 W. The Q-switch was used both to pulse the lasers at speeds matched to the camera framerate

[5] The Stokes number, defined as $\mathrm{St} = (1/18)[(\rho_p - \rho_f)/\rho_f](d/\eta)^2$, where ρ_p and ρ_f are the densities of the particles and the fluid, respectively, and d is the particle diameter, measures the importance of particle inertia. In these experiments, we have Stokes numbers ranging from 10^{-5} to 10^{-3}.

Table 1. Experimental parameters. f denotes the rotation rate of the discs, u'_r is the RMS radial velocity, u'_z is the RMS axial velocity, FPS is the camera frame rate, and δt is the time between frames. These data were taken with transparent 25 μm polystyrene microspheres. We estimate that the uncertainty in ϵ is roughly 12%.

$f(Hz)$	R_λ	u'_r (ms^{-1})	u'_z (ms^{-1})	ϵ (m^{2}s^{-3})	$\eta(\mu m)$	L/η	τ_η (ms)	T_L/τ_η	FPS	δt (ms)	$\tau_\eta/\delta t$
0.30	200	0.039	0.026	7.09×10^{-4}	192	365	36.8	51	1000	1.00	37
0.43	240	0.056	0.038	2.03×10^{-3}	146	479	21.3	61	1600	0.625	34
0.62	290	0.083	0.054	6.26×10^{-3}	111	630	12.3	74	3000	0.333	37
0.90	350	0.121	0.080	2.01×10^{-2}	84	830	7.11	88	5000	0.200	36
1.29	415	0.181	0.116	6.17×10^{-2}	64	1090	4.12	106	9000	0.111	37
1.86	500	0.262	0.169	0.196	49	1433	2.39	127	27000	0.037	65
3.50	690	0.487	0.315	1.24	30	2337	0.897	176	27000	0.037	24
5.00	815	0.669	0.440	3.39	23	3087	0.544	208	27000	0.037	15

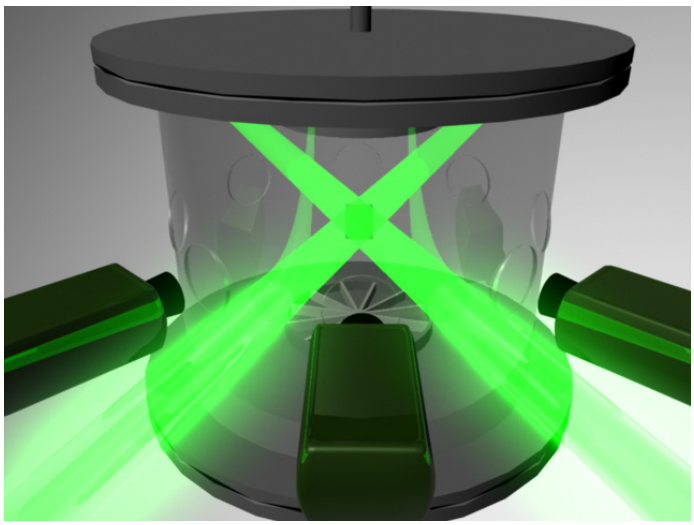

Figure 1. Sketch of the experimental setup. The three cameras have an angular separation of approximately 45° and are arranged in the forward scattering direction from both lasers.

and to increase their power. The pulse rate of both lasers was controlled by a single frequency generator. These pulses obviated the need for exact camera synchronization, since the cameras only recorded particle images while the lasers fired. Additionally, the pulse width of the lasers set the effective exposure time of the cameras, and was typically on the order of a few hundred nanoseconds. As sketched in figure 1, the cameras were placed in the forward scattering direction from each laser to maximize the amount of scattered light collected by the camera sensors.

2.3. Calibration

While particle-finding can be performed in the image space of each camera, the stereomatching and subsequent particle tracking steps require knowledge of the locations of the particle centres

Figure 2. Images of the calibration mask from each of the three cameras.

in real space. To construct the mapping between image space and real space, we use the camera calibration method developed by Tsai [14].

This method involves the fitting of nine parameters for each camera. We can map the coordinates of a particle in our experiment into the reference frame of the camera with a rotation and a translation, introducing six parameters. We also must find the effective focal length of the camera. Finally, we allow for possible radial distortion of the images, quantified with a single parameter, and a possible mismatch in the vertical and horizontal spacing of the pixels on the detector. To fit these parameters, we mount a regular dot pattern with a known spacing on a micrometre stage in the water-filled apparatus and image it with each camera at several locations. Sample images of the calibration mask are shown from each camera in figure 2. The coordinates of the dots allow the determination of the camera parameters via Tsai's model [14], which in turn allow us to find the three-dimensional coordinates of the tracer particles.

2.4. Experimental parameters

The parameters of our experiments are shown in table 1. Velocities were calculated from the particle tracks by convolution with a Gaussian smoothing and differentiating kernel as described by Mordant *et al* [15]. The energy dissipation rate ϵ was measured from the Eulerian second-order velocity structure function. Defining the Eulerian velocity increment as $\delta\mathbf{u}(\mathbf{r}) = \mathbf{u}(\mathbf{x}+\mathbf{r}) - \mathbf{u}(\mathbf{x})$, the structure function is given by $D_{ij}^{\mathrm{E}} \equiv \langle \delta u_i(\mathbf{r}) \delta u_j(\mathbf{r}) \rangle$. As is common, we split the structure function into a longitudinal component D_{LL} measured along the separation direction and a transverse component D_{NN} measured orthogonal to $\mathbf{r}$. In the inertial range,

$$D_{\mathrm{LL}}(r) = C_2(\epsilon r)^{2/3}, \tag{2}$$

and

$$D_{\mathrm{NN}} = \tfrac{4}{3} C_2(\epsilon r)^{2/3}, \tag{3}$$

where C_2 is a constant with a well-known value of 2.13 ± 0.22 [16]. By measuring the structure functions, we have determined ϵ [17]. The other parameters in table 1 are found by simple scaling arguments.

3. Turbulent relative dispersion

In a turbulent flow, a pair of fluid elements separated by a distance smaller than the integral length scale L should undergo superdiffusive separation. Once the separation of the pair has grown to the integral scale, the mean-square separation is again expected to be diffusive, i.e., grow linearly in time. When the pair separation is smaller than the Kolmogorov scale, the mean-square separation should grow exponentially [18], but when the separation lies in the inertial range we expect power-law growth rates. Richardson suggested that the mean-square separation should grow as t^3 [3]; subsequently, Obukhov refined Richardson's ideas [19] using Kolmogorov's scaling theory [2] to write

$$\langle r^2 \rangle = g\epsilon t^3, \tag{4}$$

where r is the separation of the pair, ϵ is the energy dissipation rate per unit mass, and g is termed the Richardson constant. Equation (4) is known as the Richardson–Obukhov law. Despite significant efforts, there has been no unambiguous observation of the Richardson–Obukhov law, and estimates of the Richardson constant span a full order of magnitude [18].

The Richardson–Obukhov law is the only choice consistent with Kolmogorov's scaling theory [2] when the separation time is considered to be the only relevant parameter. As Batchelor [4] realized, however, if the initial pair separation r_0 is accounted for, a second scaling law can be obtained. With r_0 in the problem, we have four independent parameters ($\langle r(t)^2 \rangle$, r_0, t, and ϵ) and only two independent units (length and time). Using the Buckingham π-theorem [20], it follows that

$$\frac{\langle r(t)^2 \rangle}{r_0^2} = f(t/t_0), \tag{5}$$

for some function f, where

$$t_0 \equiv \left(\frac{r_0^2}{\epsilon} \right)^{1/3}. \tag{6}$$

t_0, the classical correlation time of an eddy of size r_0, is the time for which a particle pair 'remembers' its initial separation.

Let us define $t^* \equiv t/t_0$, and consider the derivative of the mean-square separation with respect to t^*,

$$\frac{\mathrm{d}}{\mathrm{d}t^*} \frac{\langle r(t^*)^2 \rangle}{r_0^2} = \frac{2\langle r_i(t^*) \delta u_i(t^*) \rangle}{r_0^2}, \tag{7}$$

where $\delta u(t^*)$ is the relative velocity of the two fluid elements and summation over repeated indices is implied. Using the fundamental theorem of calculus, we can rewrite this expression as

$$\frac{\mathrm{d}}{\mathrm{d}t^*} \frac{\langle r(t^*)^2 \rangle}{r_0^2} = \frac{2}{r_0^2} \left\{ \langle r_{0i} \delta u_i(t^*) \rangle + \int_0^{t^*} \langle \delta u_i(t^*) \delta u_i(t') \rangle \, \mathrm{d}t' \right\}. \tag{8}$$

In his original work, Batchelor set $\langle r_{0i} \delta u_i(t^*) \rangle$ to zero, reasoning that the initial separation and the relative velocity should be uncorrelated [4]. As we show later, however, this assumption does not appear to hold for our data, and we have therefore kept this term in our calculations.

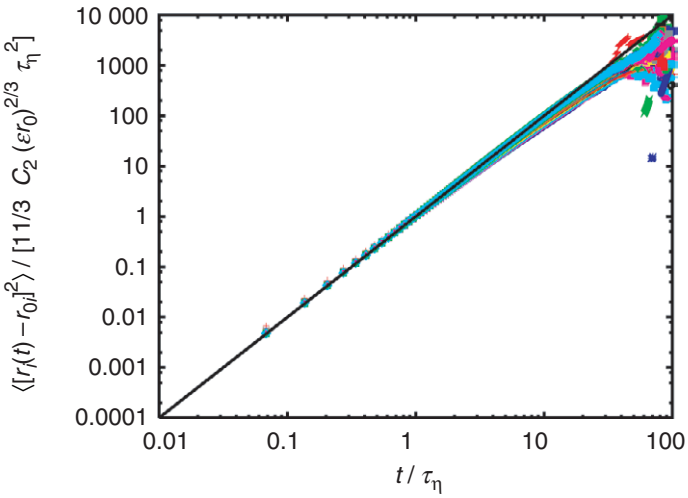

Figure 3. Scale collapse of the mean-square particle separation at $R_\lambda = 815$. The relative dispersion $\langle |\mathbf{r}(t) - \mathbf{r}_0|^2 \rangle$ scaled by $(11/3)C_2(\epsilon r_0)^{2/3}$ is plotted for 50 different bins of initial separations, ranging from 0–1 mm ($\approx$0–43η) to 49–50 mm ($\approx$2107–2150η). The solid line is a pure t^2 power law, and is not a fit. The data collapse on to the t^2 law almost perfectly [21].

For $t^* \ll 1$, corresponding to $t \ll t_0$, the relative velocity changes slowly and we can approximate

$$\langle \delta u_i(t^*) \delta u_i(t') \rangle \approx \langle \delta u(0)^2 \rangle, \tag{9}$$

which is equivalent to $\langle \delta u(r_0)^2 \rangle$, the trace of the second-order Eulerian velocity structure function tensor. Integrating (8) and grouping terms, we therefore have

$$\langle |\mathbf{r}(t) - \mathbf{r}_0|^2 \rangle = \tfrac{11}{3} C_2 (\epsilon r_0)^{2/3} t^2, \tag{10}$$

where C_2 is again the scaling constant for the second-order Eulerian velocity structure function. This expression, which we term Batchelor scaling, should hold for $t \ll t_0$. For $t \gg t_0$, the initial separation should no longer be a relevant parameter, and the particle pair is expected to obey the Richardson–Obukhov law. Combining Batchelor's scaling law with the Richardson–Obukhov law, we can write the evolution of the mean-square pair separation in the inertial range as

$$\langle |\mathbf{r}(t) - \mathbf{r}_0|^2 \rangle = \begin{cases} \tfrac{11}{3} C_2 (\epsilon r_0)^{2/3} t^2, & t \ll t_0, \\ g \epsilon t^3, & t_0 \ll t \ll T_L, \end{cases} \tag{11}$$

where T_L is the integral timescale.

We have previously reported the observation of a clear Batchelor scaling range at Reynolds numbers up to $R_\lambda = 815$ [21]. When we plot $\langle |\mathbf{r}(t) - \mathbf{r}_0|^2 \rangle$ scaled by Batchelor's constant $(11/3)C_2(\epsilon r_0)^{2/3}$, we see a collapse of the dispersion data for different initial separations on to a t^2 power law with unit slope, as illustrated in figure 3 at $R_\lambda = 815$. Plotted in this fashion, with time nondimensionalized by the Kolmogorov time τ_η, the data for each initial separation deviates from

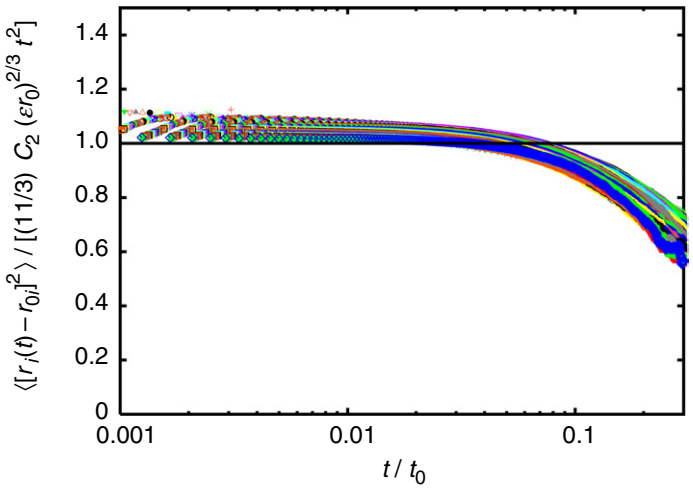

Figure 4. Compensated mean-square pair separation with timescaled by t_0. Plotted in this way, the data collapse in both space and time [21].

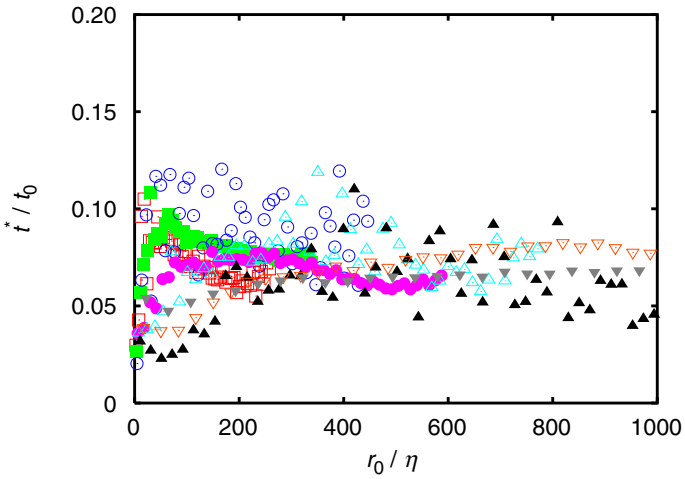

Figure 5. Deviation from Batchelor's prediction. We define t^* to be the time when the data deviate by more than 5% from Batchelor's prediction. t^*/t_0 is shown for eight different Reynolds numbers: $R_\lambda = 200$ (□), 240 (■), 290 (○), 350 (●), 415 (△), 500 (▲), 690 (▽), and 815 (▼).

the Batchelor prediction at a different time. When we scale time instead by Batchelor's timescale $t_0 = (r_0^2/\epsilon)^{1/3}$, the data collapse in both space and time. This is shown in figure 4, where the data is now compensated by $(11/3)C_2(\epsilon r_0)^{2/3}t^2$ to show the quality of the scale collapse. For each initial separation, the data deviate from Batchelor's prediction at approximately the same value of (t/t_0). We define t^* to be the time when the data deviate by 5% from the Batchelor prediction. As shown in figure 5, $t^* = (0.071 \pm 0.009)t_0$ for the entire range of Reynolds numbers tested. Currently, we do not have enough data at very long times to see the scaling behaviour at times longer than t_0; we hope to measure this behaviour in the future.

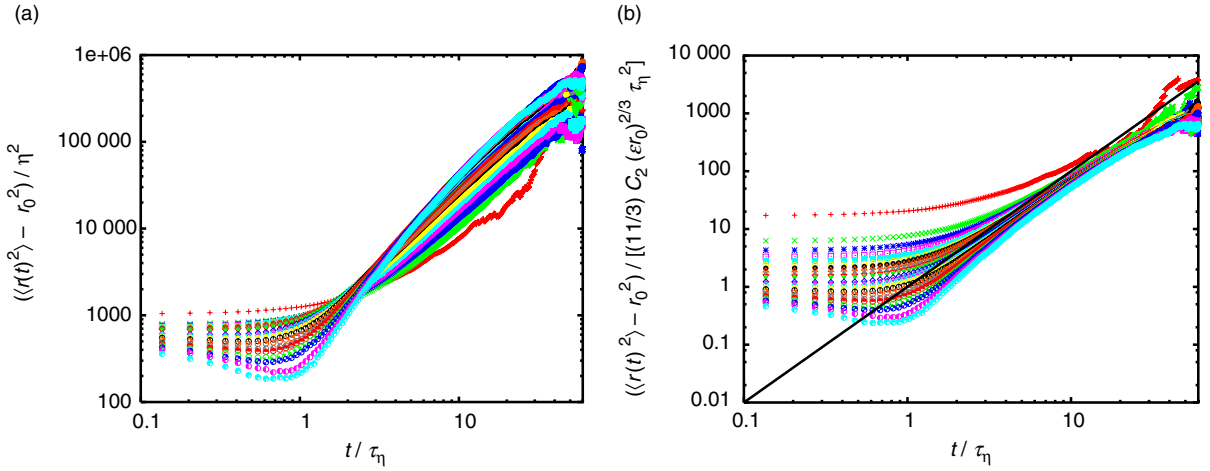

Figure 6. Batchelor's original measure of relative dispersion at $R_\lambda = 815$. No universal behaviour is seen for the different initial separations. Panel (a) shows the raw dispersion data, while (b) shows an attempt to collapse the data with Batchelor's scaling prediction.

As we mentioned above, in Batchelor's original work [4], he considered the quantity $[\langle r(t)^2\rangle - r_0^2]$ rather than the $\langle|\mathbf{r}(t) - \mathbf{r}_0|^2\rangle$ we have shown here. The difference between the two is the correlation between the initial separation and the relative velocity of the pair, which he assumed to be negligible. This must not be the case, however, since when we compute $[\langle r(t)^2\rangle - r_0^2]$, as shown in figure 6, we do not find clean, universal scaling behaviour. By the same token, we do not see clean scaling when we plot $\langle r(t)^2\rangle$ without removing the initial separation. Similar non-universal behaviour for these quantities is evident in direct numerical simulations of relative dispersion [22].

We note here that our results are in some sense surprising, given the large-scale inhomogeneity and anisotropy present in our flow. It appears that the Batchelor t^2 law is therefore very robust, and should be present in other real-world flows that are not perfectly homogeneous and isotropic.

4. Higher-order statistics

We have shown in figures 4 and 5 that the mean-square pair separation deviates from the Batchelor prediction at a universal time of roughly $0.071t_0$. This turnover cannot be a transition to Richardson–Obukhov scaling, since the Richardson constant g is assumed to be positive: the Richardson–Obukhov regime accelerates the dispersion, while the deviation from the Batchelor law we have found corresponds to slower dispersion. We have therefore investigated the possibility that this deviation is a manifestation of higher-order corrections to Batchelor's law. Let us consider the Taylor expansion of $\langle|\mathbf{r}(t) - \mathbf{r}_0|^2\rangle$ in time. To third order, this expansion gives

$$\langle|\mathbf{r}(t) - \mathbf{r}_0|^2\rangle \approx \langle\delta\mathbf{u}(r_0)\cdot\delta\mathbf{u}(r_0)\rangle t^2 + \langle\delta\mathbf{u}(r_0)\cdot\delta\mathbf{a}(r_0)\rangle t^3, \tag{12}$$

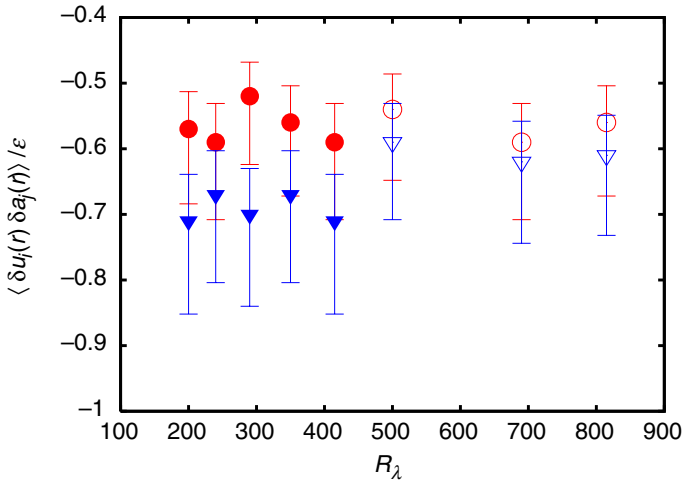

Figure 7. Longitudinal (●) and transverse (▼) scaling constants for the Eulerian mixed velocity–acceleration structure function. The magnitude of the transverse component shrinks for $R_\lambda > 500$, possibly due to poor resolution of the acceleration at high Reynolds number. We have therefore plotted these points using open symbols. Even at these high Reynolds numbers, we note that the velocity and position statistics should be well-resolved. Error bars were estimated using the methodology given in [6].

where $\delta\mathbf{u}$ and $\delta\mathbf{a}$ are the relative velocity and acceleration of the two particles, respectively. The zero- and first-order terms of the expansion drop out, as they must, and the second-order term is exactly the Batchelor prediction.

The coefficient of the third-order term is the trace of the Eulerian mixed velocity–acceleration structure function tensor evaluated at r_0. Since r_0 is in the inertial range, we must construct the K41 scaling law for this quantity. $\langle \delta u(r) \delta a(r) \rangle$ has the same dimensions as the dissipation rate ϵ, and so should be constant and proportional to ϵ in the inertial range. Recently, Hill [23], building on earlier work of Mann *et al* [24], has shown from the Navier–Stokes equations that

$$\langle \delta\mathbf{u}(r_0) \cdot \delta\mathbf{a}(r_0) \rangle = -2\epsilon \tag{13}$$

in the inertial range, assuming only local homogeneity. We have investigated this velocity–acceleration structure function, and have found that, as expected, it is constant in the inertial range. Just as with the Eulerian velocity structure function, we split $\langle \delta u_i(r) \delta a_j(r) \rangle$ into longitudinal and transverse components, as shown in figure 7 as a function of Reynolds number. Above $R_\lambda = 500$, the transverse component decreases in magnitude, most likely due to poorer resolution of the acceleration. The trace of $\langle \delta u_i(r) \delta a_j(r) \rangle$ is near -2 for low Reynolds numbers, as shown in figure 8, and is nearer to -1.8 for higher Reynolds numbers, since the transverse component is smaller. We note that it is only the acceleration that is under-resolved at high Reynolds numbers: the position and velocity data should be accurate. In any case, since $\langle \delta u_i(r) \delta a_i(r) \rangle$ is always negative, it is conceivable that this term may account for the deviation of the data shown in figure 4, since it tends to slow the relative dispersion.

We have replotted the data shown in figure 4 in figure 9 and have compared them with the third-order Taylor expansion discussed above. While the model has the same downward trend in

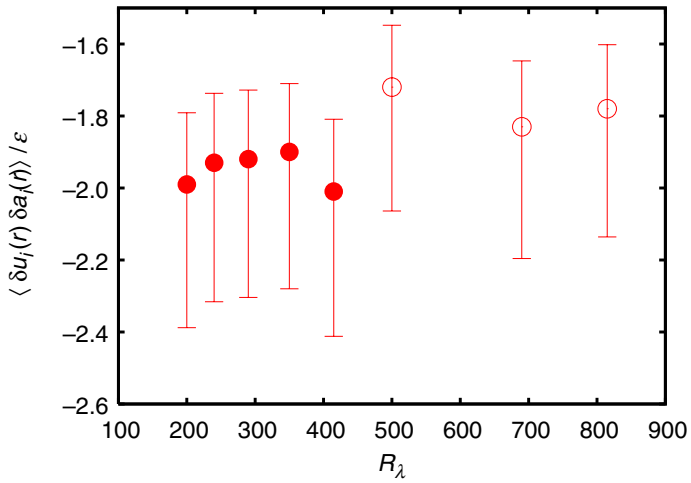

Figure 8. Trace of the Eulerian mixed velocity–acceleration structure function as a function of Reynolds number. At low Reynolds number, the trace is clustered near -2, while for higher Reynolds numbers it is closer to -1.8. The change is primarily due to the smaller transverse scaling constant. Again, we plot the high Reynolds number results using open symbols since the acceleration may be poorly resolved.

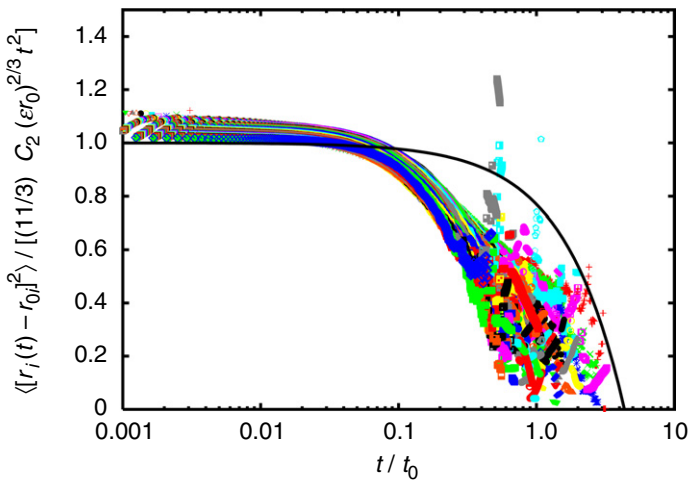

Figure 9. The same data shown in figure 4 shown with the Batchelor prediction augmented with the third-order correction (solid line). The new model captures the trend of the deviation, but is not quantitatively correct.

the compensated plot as the data, it deviates later. In order to bring the model closer to the data, the trace of $\langle \delta \mathbf{u}(r_0) \cdot \delta \mathbf{a}(r_0) \rangle$ would have to be roughly five times larger. It is therefore more likely that the deviation of our data is due to the influence of the large scales, as the relative dispersion moves into the linear Taylor regime [25]. There is also the possibility that the deviation of our data is due to a bias caused by our finite measurement volume.

5. Distance neighbour function

In Richardson's seminal paper [3], he suggested that turbulent relative dispersion can be described by a diffusion equation, albeit one where the diffusion constant $K(r, t)$ is a function of space and time. With the additional assumption that the flow is isotropic, the equation can be reduced to a single spatial dimension, namely

$$\frac{\partial}{\partial t}q(r,t) = \frac{1}{r^2}\frac{\partial}{\partial r}\left[r^2 K(r,t)\frac{\partial q(r,t)}{\partial r}\right]. \tag{14}$$

$q(r, t)$, which Richardson called the distance neighbour function, represents the spherically averaged PDF of the relative dispersion. Assuming the boundary conditions $q(\infty, t) = 0$ and $q(r, \infty) = 0$, (14) admits a self-similar solution if we additionally assume the initial condition $q(r, 0) = \delta(r)$, i.e., diffusion from a point source. Under these conditions, Richardson [3] showed that

$$q_R(r,t) = \frac{429}{70}\sqrt{\frac{143}{2}}(\pi\langle r^2\rangle)^{-3/2}\exp\left[-\left(\frac{1287r^2}{8\langle r^2\rangle}\right)^{1/3}\right], \tag{15}$$

by assuming that $K(r, t) \sim r^{4/3}$, based on measurements of diffusion constants in systems ranging from volcanoes and cyclones to molecular diffusion. Subsequently, Batchelor proposed instead that $K(r, t) \sim t^2$ [26], leading to

$$q_B(r,t) = \left(\frac{2\pi}{3}\langle r^2\rangle\right)^{-3/2}\exp\left[-\frac{3}{2}\frac{r^2}{\langle r^2\rangle}\right]. \tag{16}$$

Both of these expressions for the distance neighbour function imply a t^3 law for $\langle r^2\rangle$; indeed, any $K(r, t) \sim r^\alpha t^\beta$ that is consistent dimensionally and with K41 leads to $\langle r^2\rangle \sim t^3$ [27].

The two solutions to (14) given above both require that the fluid element pairs were at the same place at $t = 0$. We cannot replicate this condition in the laboratory. We can attempt to approximate it, however, by subtracting the initial separation of each particle pair componentwise and considering $q(\Delta r, t)$, where we define $\Delta r = |\mathbf{r} - \mathbf{r}_0|$. This approach has the perhaps unwelcome side effect of treating all pairs in the same fashion, whether they are separating or coming closer together. Since some pairs will first move closer before separating [28], simply subtracting the initial pair separation may not capture all the physics of pair separation.

Our measurements of $q(\Delta r, t)$ are shown in figure 10 for six different initial separations at $R_\lambda = 815$. For each initial separation, the distance neighbour function is shown for 20 different times ranging from τ_η to $20\tau_\eta$. For small initial separations ($<40\eta$), the measured distance neighbour function agrees well with Richardson's predicted form, while for large initial separations ($>1100\eta$), the data agree well with Batchelor's form. We show the relative deviation, defined as the difference between the predicted value and the measured value scaled by the predicted value, from Richardson's and Batchelor's forms, respectively, for the smallest and largest initial separations considered in figure 11. For intermediate initial separations, the data lie between the two predictions and undergo a transition between the two laws.

The same qualitative trend is seen at all Reynolds number investigated. We show the distance neighbour function measured at $R_\lambda = 200$ in figure 12. Again, as the initial separation increases, the data undergo a transition from Richardson's prediction to Batchelor's. $q(\Delta r, t)$ is self-similar

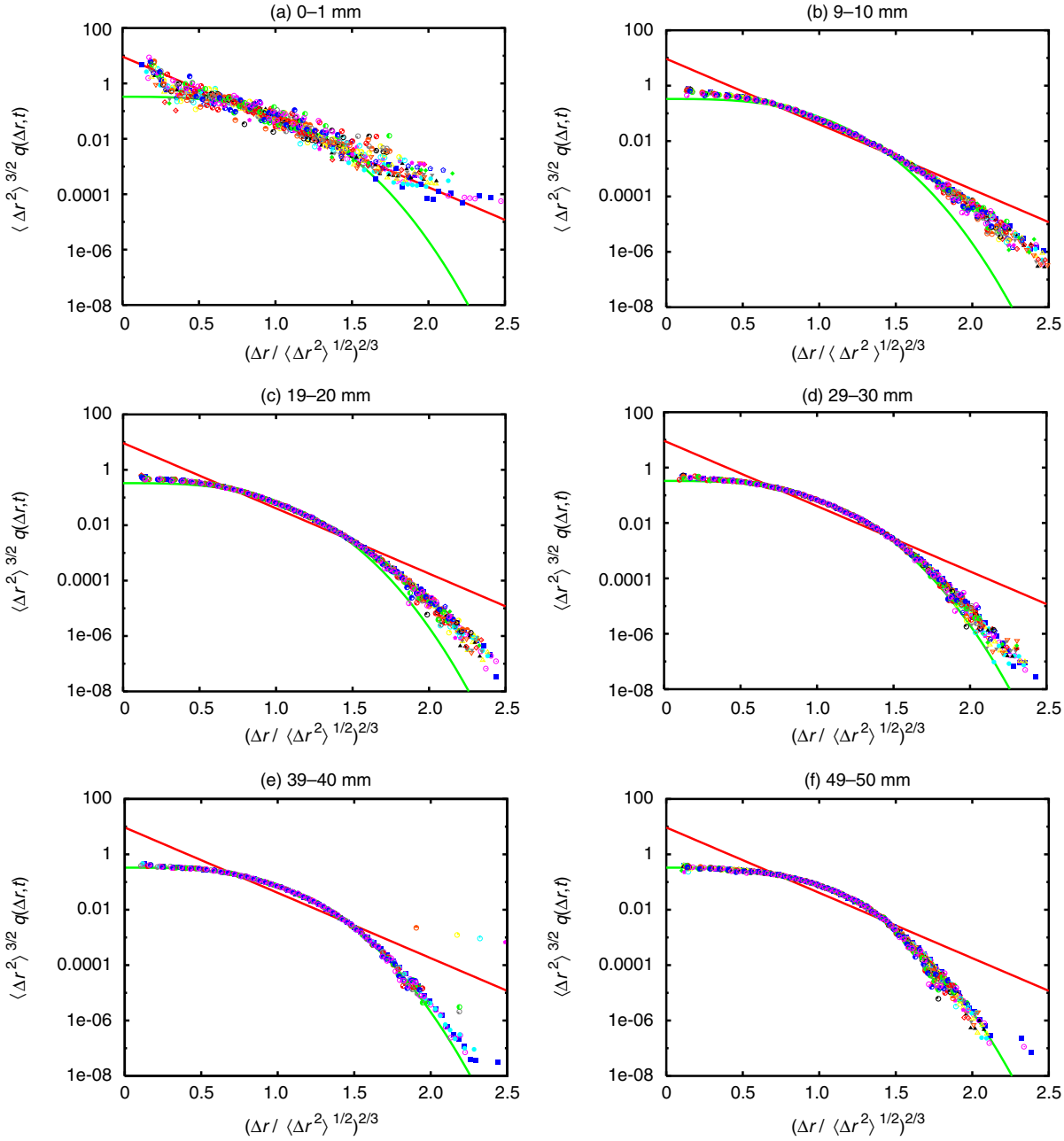

Figure 10. The distance neighbour function for different initial separations at $R_\lambda = 815$. The red straight line is Richardson's predicted PDF, while the green curved line is Batchelor's. The symbols show the experimental measurements. Each plot shows a different initial separation; for each initial separation, PDFs from 20 times ranging from τ_η to $20\tau_\eta$ are shown.

in t for all Reynolds numbers measured. We show the deviation from the Richardson and Batchelor distance neighbour function predictions for the $R_\lambda = 200$ data in figure 13.

This is not the case if we consider $q(r, t)$ without accounting for the nonzero initial separation of the pair. As shown in figure 14, the raw distance neighbour function is strongly peaked around the root-mean-square separation for short times. As time increases, $q(r, t)$ spreads out, appearing

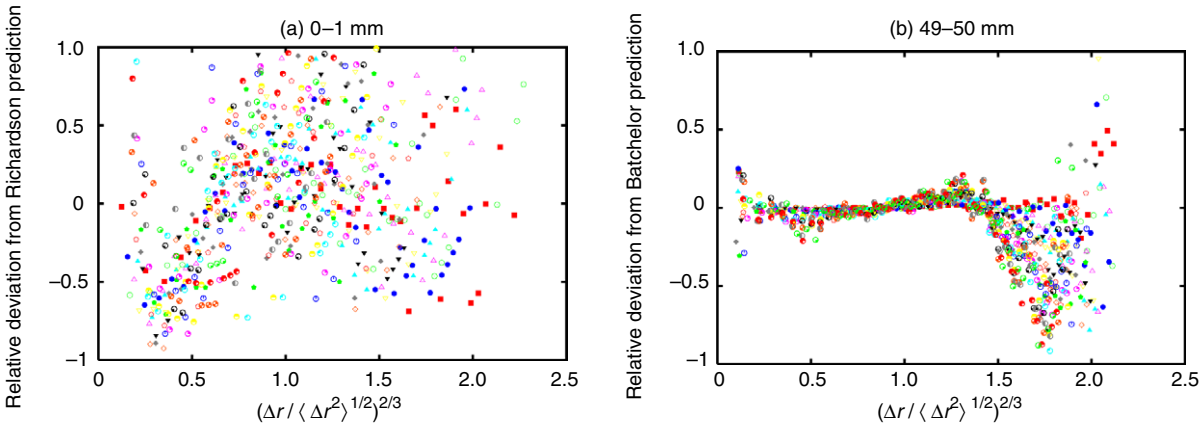

Figure 11. The relative deviation from (a) Richardson's prediction for the distance neighbour function, for small initial separations, and (b) Batchelor's prediction, for large initial separations, both at $R_\lambda = 815$.

to approach the Batchelor prediction at long times regardless of the initial separation. It remains unclear whether this approach is more justified for calculating the distance neighbour function when faced with a real, physical situation where the pairs are not dispersing from a point source or whether the initial separation should be removed. We also note that our large-scale flow is neither homogeneous nor isotropic, while standard solutions of the Richardson diffusion equation assume isotropy.

6. Fixed-scale statistics

As we have shown in section 3, we did not observe the Richardson–Obukhov law in its original form even at Reynolds numbers as high as $R_\lambda = 815$; instead, we observed a regime consistent with Batchelor's predictions throughout most of our inertial range with initial separations also lying in the inertial range. This behaviour suggests that a much higher Reynolds number may be required before the Richardson–Obukhov prediction can be unambiguously observed in its original form. The appeal of the Richardson–Obukhov law, though, seeing as it should be universal for all particle pairs with only a single free parameter, has led researchers to introduce new statistics in the hope that behaviour consistent with it may be found at the moderate Reynolds numbers reached in experiments and simulations. One such quantity, the average $\langle r^{2/3} \rangle$, was shown by Bourgoin *et al* [21]. Instead of studying different averages of the pair separation as a function of time, however, one can also study averages of the time it takes for the pair separation to grow to a particular threshold. These so-called fixed-scale statistics are averaged over an ensemble of pairs at a fixed spatial scale rather than at a fixed temporal scale as in the traditional Richardson–Obukhov or Batchelor descriptions of turbulent relative dispersion [29]. Dimensionally, a scaling law such as

$$\langle t \rangle = G\epsilon^{-1/3} r^{2/3} \tag{17}$$

is consistent with the Richardson–Obukhov law.

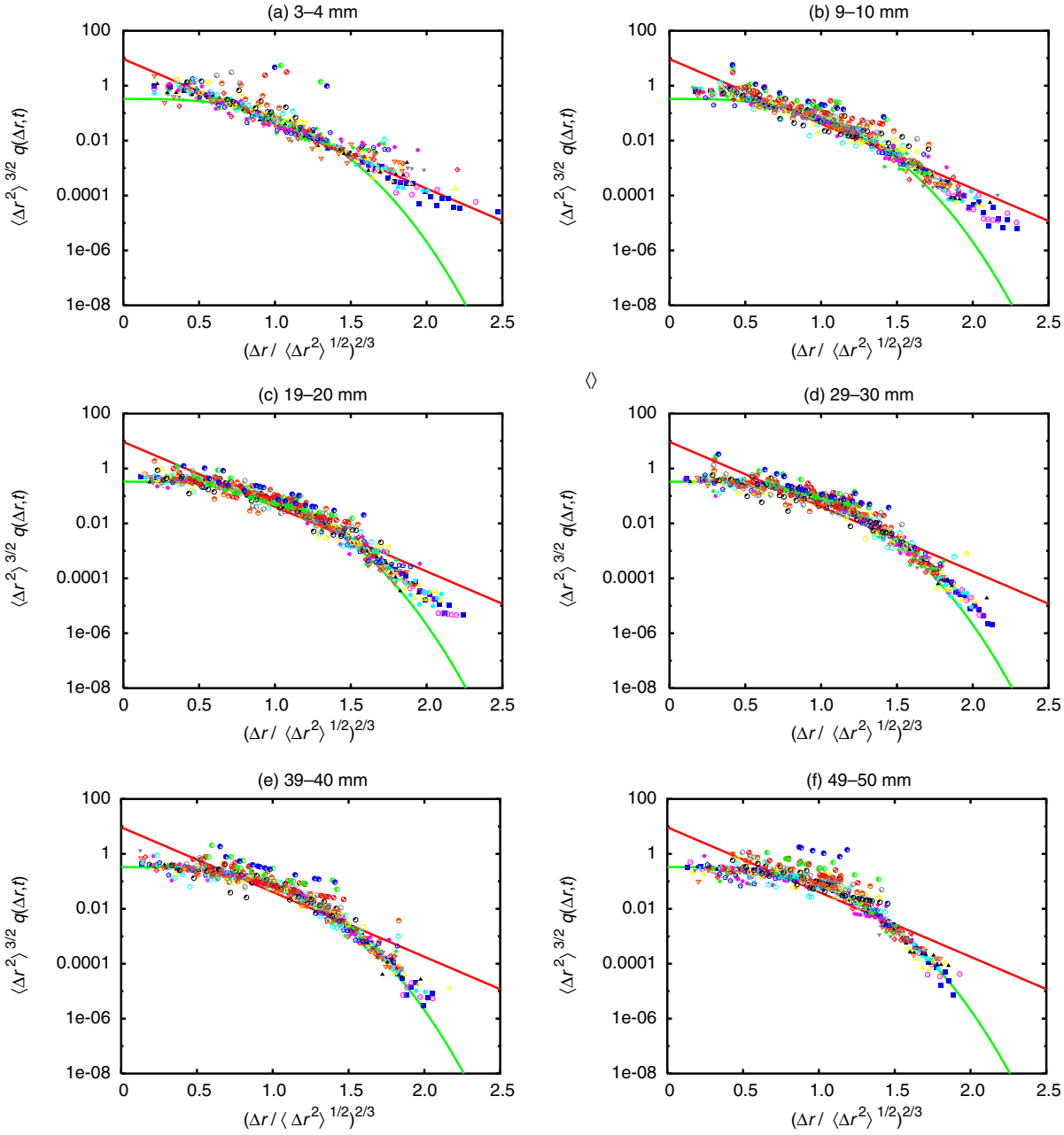

Figure 12. The distance neighbour function for different initial separations at $R_\lambda = 200$. The red line is again Richardson's PDF, while the green line is Batchelor's. The symbols are the experimental measurements. While the data are much noisier, the same qualitative trends as in the $R_\lambda = 815$ data are evident. Here, 1 mm $\approx 5\eta$.

The most well-known fixed-scale statistics are the exit time or doubling time statistics introduced by Artale *et al* [30]. In an exit time analysis, one defines a set of thresholds r_n for every particle pair such that

$$r_n = \rho^n r_0, \tag{18}$$

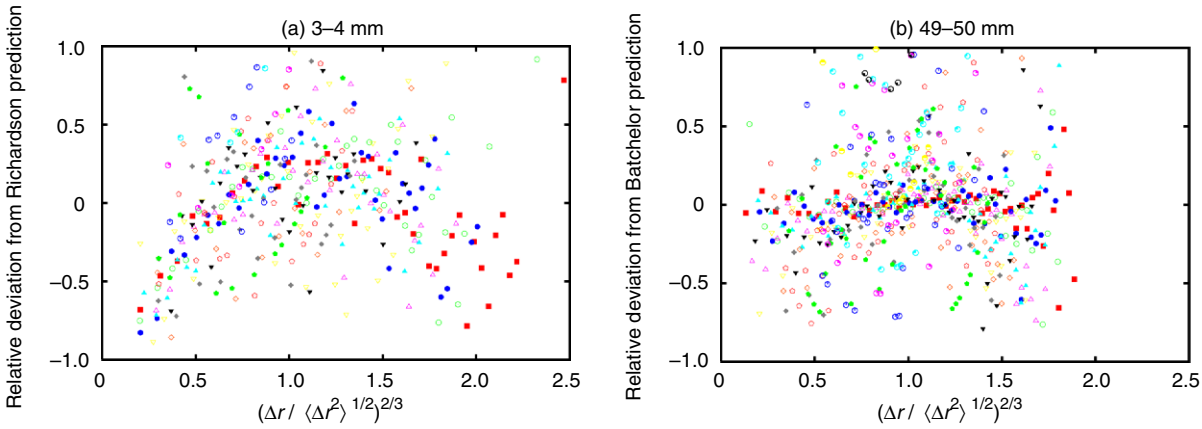

Figure 13. The relative deviation from (a) Richardson's prediction for the distance neighbour function, for small initial separations, and (b) Batchelor's prediction, for large initial separations, both at $R_\lambda = 200$.

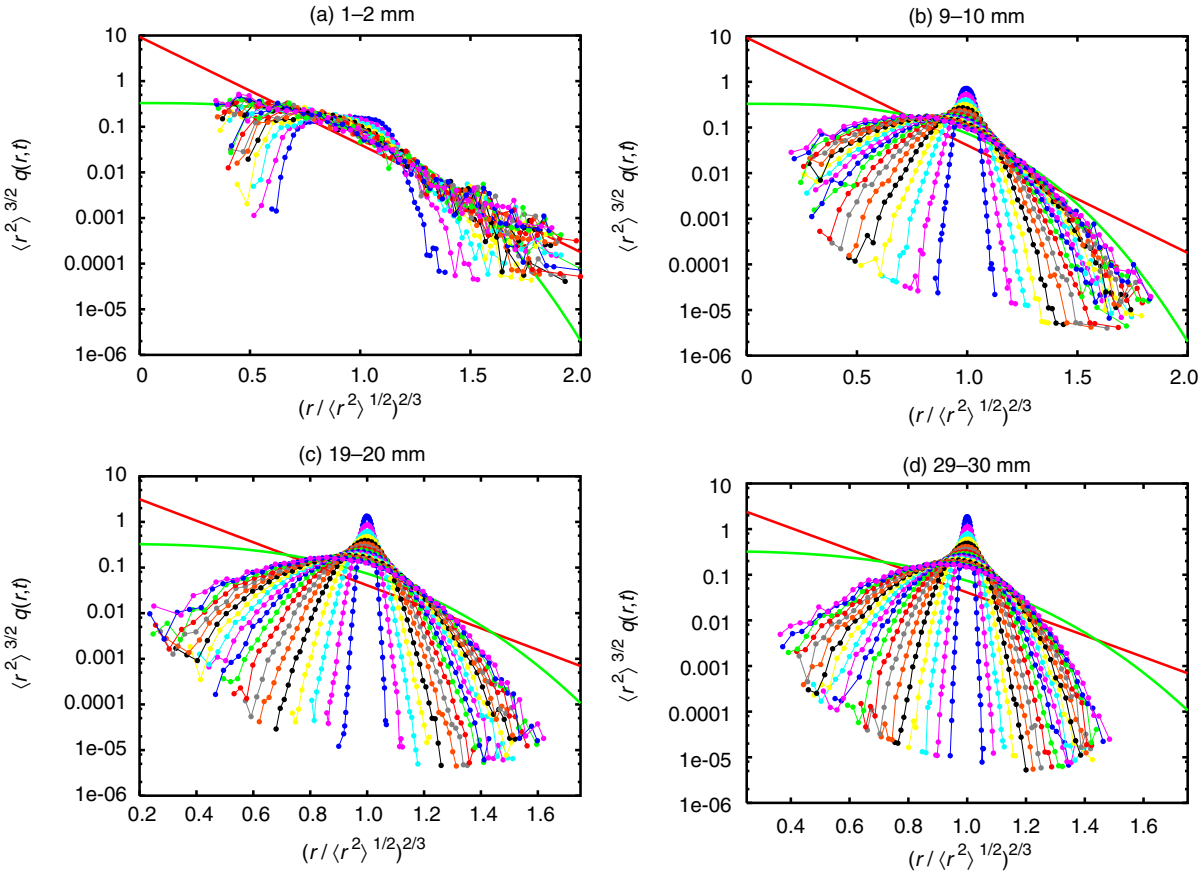

Figure 14. The distance neighbour function for different initial separations at $R_\lambda = 815$ without subtracting the initial separation. The red line is again Richardson's PDF, while the green line is Batchelor's. The short time data are peaked near the root-mean-square separation. The measured PDFs spread as time increases, approaching the Batchelor PDF.

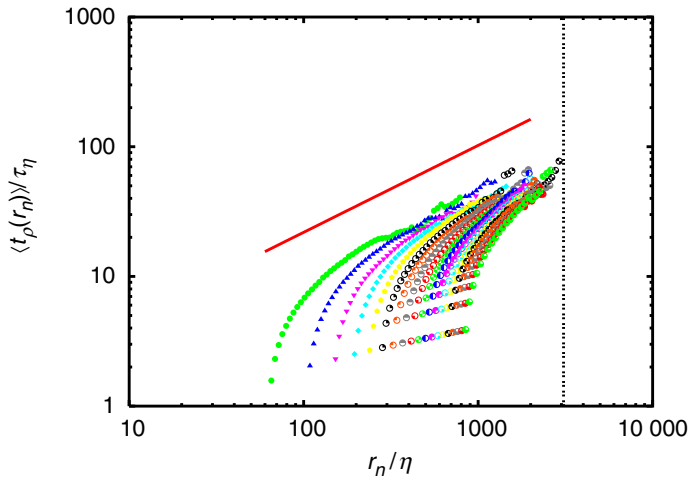

Figure 15. Average exit times at $R_\lambda = 815$ with $\rho = 1.05$. The solid line is an $r_n^{2/3}$ power law for reference. From left to right, the symbols correspond to 1 mm wide bins of initial separations ranging from 1–2 mm (43–86η) to 19–20 mm (817–860η). The dashed line on the right corresponds to the integral length scale.

where $\rho > 1$ is a scale factor. The exit time $t_\rho(r_n)$ is then defined to be the time it takes for the separation of the particle pair to grow from r_n to r_{n+1}. For the case of $\rho = 2$, $t_2(r_n)$ is the time it takes for the pair to double in size. Exit time statistics have recently been proposed as a powerful alternative to the traditional analyses of turbulent relative dispersion, and it has been suggested that they should show 'true' inertial range scaling behaviour (i.e., behaviour consistent with the Richardson–Obukhov law) even at moderate Reynolds numbers [22], [29]–[31].

Dimensionally, $\langle t_\rho(r_n)\rangle \sim r_n^{2/3}$. Without additional assumptions, however, this exit time analysis cannot be compared with the traditional metrics of relative dispersion. To overcome these difficulties, Boffetta and Sokolov [31] assumed the Richardson form for the distance neighbour function and showed that

$$\langle t_\rho(r_n)\rangle = \left(\frac{143}{81}(g\epsilon)^{-1}\right)^{1/3} \frac{\rho^{2/3}-1}{\rho^{2/3}} r_n^{2/3}. \tag{19}$$

This expression can be inverted to give an expression for the Richardson constant g in terms of the ensemble average of the exit times, namely

$$g = \frac{143}{81}\frac{(\rho^{2/3}-1)^3}{\rho^2}\frac{r_n^2}{\epsilon\langle t_\rho(r_n)\rangle^3}. \tag{20}$$

We have performed an exit time analysis of our data with $\rho = 1.05$; ρ was chosen so that we could see a long series of data. The results are shown in figure 15 for several different initial separations at $R_\lambda = 815$. There is no clear collapse of the data for different initial separations, although the scaling range increases as the initial separation decreases. At larger scales, the data may be approaching an $r_n^{2/3}$ power law as predicted by Boffetta and Sokolov [31], though these scales are also very close to the integral length scale, beyond which there should be no superdiffusive behaviour.

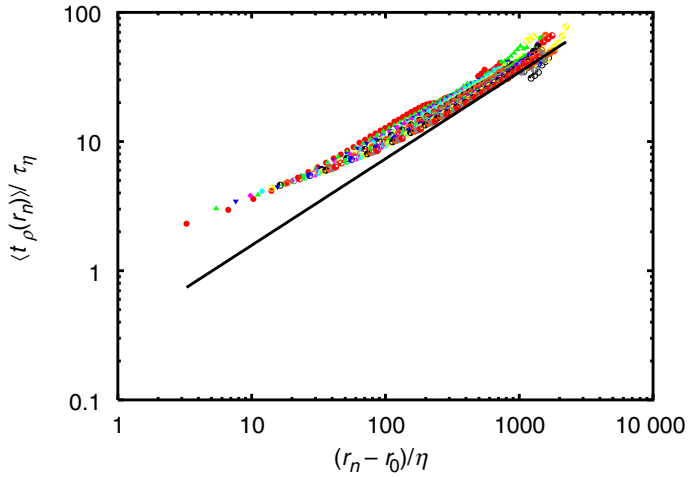

Figure 16. Average exit times with the initial separation subtracted at $R_\lambda = 815$ with $\rho = 1.05$. The solid line is again a reference $r_n^{2/3}$ power law. The symbols are the same as those in figure 15.

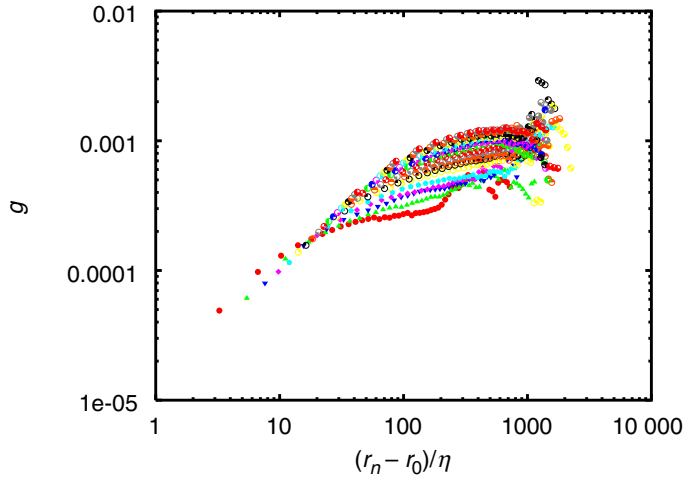

Figure 17. The Richardson constant computed from the exit times with the initial separation subtracted at $R_\lambda = 815$. No initial-separation-independent plateau is seen.

Just as we did with the distance neighbour function, we have also attempted to account for the finite initial separations in our data by subtracting off r_0 componentwise from the exit time data. These results are shown in figure 16, again at $R_\lambda = 815$ and with $\rho = 1.05$. With this modification to the model, our results appear similar to those of Biferale *et al* [22], who investigated relative dispersion in a direct numerical simulation of the Navier–Stokes equations. Though Biferale *et al* [22] did not remove their initial separations, they considered only initial separations of less than 20η. With r_0 that small, initial separation effects may be negligible. We, however, do not have enough data at initial separations of that scale with which to test this hypothesis.

Equation (20) can be used to extract the Richardson constant from an exit time analysis, subject to the assumptions outlined above. We show this mapping in figure 17 for the exit time

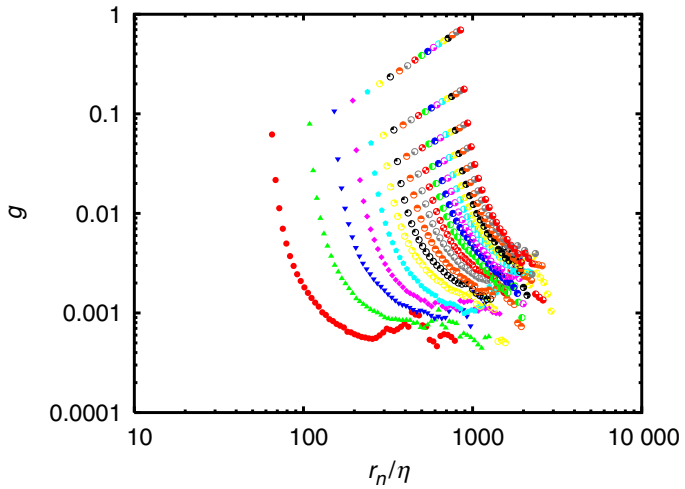

Figure 18. The Richardson constant computed from the exit times without subtracting the initial separation at $R_\lambda = 815$. No plateau is seen.

analysis with the initial separations subtracted. Biferale *et al* [22] report that this analysis shows a plateau in the Richardson constant with a value of $g \approx 0.5$. We, however, see different behaviour. While the data does begin to flatten, there is no universal value of g observed. In addition, the putative Richardson constant we find is two orders of magnitude smaller than that of Biferale *et al*. If we instead plot the Richardson constant without subtracting the initial separation, as shown in figure 18, no plateau is seen.

The apparent scaling found by Biferale *et al* may be attributable to the small initial separations used in their simulations. Here, we have measured initial separations in the inertial range, since the original Richardson and Batchelor predictions are inertial range theories. For the separations investigated in our experiments, we do not see a clear scale collapse.

7. Conclusions

We have measured the spreading of pairs of passive tracer particles in an intensely turbulent water flow, and have tested several models of turbulent relative dispersion. We find no traditional Richardson–Obukhov scaling, but do find excellent agreement with Batchelor's predictions that treat the initial pair separation as an important parameter. We find that Batchelor's timescale t_0 accurately quantifies the persistence of the Batchelor scaling regime, and that deviations from the Batchelor law are not due to higher-order corrections. We have shown measurements of the distance neighbour function, the PDF of relative dispersion, and have found that it appears to undergo a transition between Richardson's form and Batchelor's form when we remove the initial separation. We have also investigated the recently proposed exit time statistics, and have found that they do not appear to fit our data accurately. Finally, we note that our experiments were conducted in a flow that is neither homogeneous nor statistically isotropic. Since our measurement volume was large enough that some of our data comes nearly an integral scale away from the point of highest symmetry in our flow, our results appear to be robust to these non-idealities. Nevertheless, we look forward to experiments conducted in other flows to compare with our results.

Acknowledgments

This work was supported by the NSF under grants PHY-9988755 and PHY-0216406 and by the Max Planck Society.

References

[1] Feynman R P, Leighton R B and Sands M L 1963 *The Feynman Lectures on Physics* vol 1 (Reading, MA: Addison-Wesley)
[2] Kolmogorov A N 1941 The local structure of turbulence in incompressible viscous fluid for very large Reynolds numbers *Dokl. Akad. Nauk SSSR* **30** 301–5
[3] Richardson L F 1926 Atmospheric diffusion shown on a distance-neighbour graph *Proc. R. Soc. Lond.* A **110** 709–37
[4] Batchelor G K 1950 The application of the similarity theory of turbulence to atmospheric diffusion *Q. J. R. Meteorol. Soc.* **76** 133–46
[5] Voth G A, Satyanarayan K and Bodenschatz E 1998 Lagrangian acceleration measurements at large Reynolds numbers *Phys. Fluids* **10** 2268–80
[6] Voth G A, La Porta A, Crawford A M, Alexander J and Bodenschatz E 2002 Measurement of particle accelerations in fully developed turbulence *J. Fluid Mech.* **469** 121–60
[7] Gylfason A, Ayyalasomayajula S and Warhaft Z 2005 Lagrangian measurements of inertial particles in wind tunnel turbulence *Bull. Am. Phys. Soc.* **50** 65
[8] Mordant N, Metz P, Michel O and Pinton J-F 2001 Measurement of Lagrangian velocity in fully developed turbulence *Phys. Rev. Lett.* **87** 214501
[9] Ouellette N T, Xu H and Bodenschatz E 2006 A quantitative study of three-dimensional Lagrangian particle tracking algorithms *Exp. Fluids* **40** 301–13
[10] Maas H-G, Gruen A and Papantoniou D 1993 Particle tracking velocimetry in three-dimensional flows—Part 1. Photogrammetric determination of particle coordinates *Exp. Fluids* **15** 133–46
[11] Voth G A, La Porta A, Crawford A M, Bodenschatz E and Alexander J 2001 A silicon strip detector system for high resolution particle tracking in turbulence *Rev. Sci. Instrum.* **72** 4348–53
[12] La Porta A, Voth G A, Crawford A M, Alexander J and Bodenschatz E 2001 Fluid particle accelerations in fully developed turbulence *Nature* **409** 1017–19
[13] Dracos Th 1996 Particle tracking in three-dimensional space *Three-Dimensional Velocity and Vorticity Measuring and Image Analysis Techniques* ed Th Dracos (Dordrecht: Kluwer) pp 129–52
[14] Tsai R Y 1987 A versatile camera calibration technique for high-accuracy 3D machine vision metrology using off-the-shelf TV cameras and lenses *IEEE T. Robot. Autom.* **RA-3** 323–44
[15] Mordant N, Crawford A M and Bodenschatz E 2004 Experimental Lagrangian acceleration probability density function measurement *Physica* D **193** 245–51
[16] Sreenivasan K R 1995 On the universality of the Kolmogorov constant *Phys. Fluids* **7** 2778–84
[17] Ouellette N T 2006 Probing the statistical structure of turbulence with measurements of tracer particle tracks *PhD thesis* Cornell University
[18] Sawford B 2001 Turbulent relative dispersion *Annu. Rev. Fluid Mech.* **33** 289–317
[19] Obukhov A M 1941 Spectral energy distribution in turbulent flow *Izv. Akad. Nauk SSSR* **5** 453–566
[20] Buckingham E 1914 On physically similar systems; illustrations of the use of dimensional equations *Phys. Rev.* **4** 345–76
[21] Bourgoin M, Ouellette N T, Xu H, Berg J and Bodenschatz E 2006 The role of pair dispersion in turbulent flow *Science* **311** 835–38
[22] Biferale L, Boffetta G, Celani A, Devenish B J, Lanotte A and Toschi F 2005 Lagrangian statistics of particle pairs in homogeneous isotropic turbulence *Phys. Fluids* **17** 115101

[23] Hill R J 2006 Opportunities for use of exact statistical equations *J. Turbul.* at press (*Preprint* physics/0512038 at http: //www.arxiv.org)
[24] Mann J, Ott S and Andersen J S 1999 Experimental study of relative, turbulent diffusion *Technical Report Risø-R-1036 (EN), Risø National Laboratory*
[25] Taylor G I 1922 Diffusion by continuous movements *Proc. Lond. Math. Soc.* **20** 196–212
[26] Batchelor G K 1952 Diffusion in a field of homogeneous turbulence II. The relative motion of particles *Proc. Camb. Phil. Soc.* **48** 345–62
[27] Klafter J, Blumen A and Shlesinger M F 1987 Stochastic pathway to anomalous diffusion *Phys. Rev.* A **35** 3081–5
[28] Pumir A, Shraiman B I and Chertkov M 2001 The Lagrangian view of energy transfer in turbulent flow *Europhys. Lett.* **56** 379–85
[29] Boffetta G and Celani A 2000 Pair dispersion in turbulence *Physica* A **280** 1–9
[30] Artale V, Boffetta G, Celani A, Cencini M and Vulpiani A 1997 Dispersion of passive tracers in closed basins: beyond the diffusion coefficient *Phys. Fluids* **9** 3162–71
[31] Boffetta G and Sokolov I M 2002 Relative dispersion in fully developed turbulence: the Richardson's law and intermittency corrections *Phys. Rev. Lett.* **88** 094501